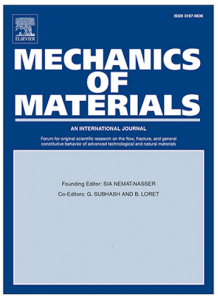

Reduced kinematic multiscale model for tissue engineering electrospun scaffolds

Daniel Enrique Caballero, Florencia Montini-Ballarin, Juan Manuel Gimenez, Nicolás Biocca, Nahuel Rull, Patricia Frontini, Santiago Adrián Urquiza

PII: S0167-6636(22)00004-7
DOI: https://doi.org/10.1016/j.mechmat.2022.104214
Reference: MECMAT 104214

To appear in: *Mechanics of Materials*

Received date : 20 May 2021
Revised date : 20 December 2021
Accepted date : 4 January 2022

Please cite this article as: D.E. Caballero, F. Montini-Ballarin, J.M. Gimenez et al., Reduced kinematic multiscale model for tissue engineering electrospun scaffolds. *Mechanics of Materials* (2022), doi: https://doi.org/10.1016/j.mechmat.2022.104214.

Reduced Kinematic Multiscale Model for Tissue Engineering Electrospun Scaffolds

Daniel Enrique Caballero[a,c], Florencia Montini-Ballarin[a,b,c], Juan Manuel Gimenez[a,c], Nicolás Biocca[a,c], Nahuel Rull[b,c], Patricia Frontini[b,c], Santiago Adrián Urquiza[a,*]

[a] *Grupo de Ingeniería Asistida por Computador (GIAC), Facultad de Ingeniería, Universidad Nacional de Mar del Plata (UNMdP), Argentina*
[b] *Instituto de Investigaciones en Ciencia y Tecnología de Materiales (INTEMA), Argentina*
[c] *Consejo Nacional de Investigaciones Científicas y Técnicas (CONICET), Argentina*

Abstract

To this day, there is still a need for a direct relationship between the microscopic material properties and network microstructure configuration with the macroscopic mechanical response in order to optimize the design loops of biomimetic electrospun grafts. Multiscale mechanical modeling arises as a useful alternative, which allows to represent the individual nanofibers mechanical response and how the interaction between fibers results in the final macroscopic behavior. In this work, a micromechanical model that accounts for fiber interaction, progressive straightening (i.e. progressive recruitment) and reorientation is presented. An RVE is generated by means of a virtual deposition algorithm that mimics the electrospinning process itself, thus obtaining geometries that resemble the observed electrospun microstructure. These geometries were then validated by comparison with analysis of SEM images, taking special interest in the diameter, orientation and tortuosity distributions. Then, an elastic-plastic constitutive law for the nanofibers is implemented along with a simplified kinematic description that results in a significant reduction of the number of Degrees of Freedom of the discretized mechanical equilibrium problem. Finally, the micromechanical model is validated against uniaxial tensile tests of electrospun PLLA bone-shaped samples, reproducing the experimentally observed behavior while employing realistic geometric and constitutive parameters to characterize the fibers.

Keywords: scaffolds, electrospinning, mechanical behavior, microstructure, multiscale modeling

* Corresponding author
Email addresses: dcaballero@fi.mdp.edu.ar (Daniel Enrique Caballero), florenciamontini@fi.mdp.edu.ar (Florencia Montini-Ballarin), jmgimenez@fi.mdp.edu.ar (Juan Manuel Gimenez), nicolas.biocca@fi.mdp.edu.ar (Nicolás Biocca), nrull@fi.mdp.edu.ar (Nahuel Rull), pmfronti@fi.mdp.edu.ar (Patricia Frontini), surquiza@fi.mdp.edu.ar (Santiago Adrián Urquiza)

1. Introduction

In the last decades, the electrospinning technique arrived as a novel processing method to produce non-woven porous matrices conformed by nanofibers [1]. The two-scale structure present in nanofibrous networks results in their versatility and improved properties. At the micrometer scale the nanofibers dimension, composition and interaction imparts unique properties, such as high area to volume ratio, ultrahigh strength-/toughness coupled with extreme flexibility [2, 3]. On the other hand, the network acts as a continuum at the macroscopic scale [4, 5]. This characteristic features of electrospun networks results in promising outcomes in different fields such as textiles, filtration, energy, sensors, aerospace, and biomedical applications, where the microscale needs to be properly tailored to match the required macromechanical specifications [1, 6]. Particularly in biomedical applications, the interaction of cells with the electrospun scaffold influences the cells morphology, adhesion, proliferation and extracellular matrix formation [7]. In addition, the macroscopic properties of the scaffold must match those of the replaced tissue in order to reduce the risk of scaffold failure due to a mechanical mismatch [8–10]. Therefore, a deeper understanding of these structures and how the nanofiber interactions results in the targeted macro-scale properties is of primary importance [11, 12]. However, since purely descriptive modeling is the most commonly used approach, still to these days the full mechanical behavior of nanofibrous scaffolds is barely understood [11, 13, 14].

When designing a scaffold for a particular application, the most common development approach involves a significant number of experimental iterations [4, 15]. Moreover, the electrospun unique microstructure, with high porosity and a fibrous network with absence of a supporting matrix, results in a very different mechanical response compared to the base material's bulk counterpart [14]. The nanofibers within the electrospun network are subjected to straightening, reorientation, frictional contact, plasticity, and damage, among others [2, 16]. These nonlinear mechanisms that nanofibers undergo during deformation are complex to measure or characterize experimentally. Therefore, it is difficult to predict the scaffold macroscopic mechanical response in relation to its microscopic properties [17].

The lack of understanding and the absence of a theoretical framework able to predict the scaffold macroscopic mechanical response in relation to its microscopic properties may prevent electrospun nanofibers from reaching their full potential [17]. Conventional development approaches often require a significant

number of experimental iterations to explicitly meet the design objectives [4, 15]. Understanding the mechanical behavior of nanofibrous scaffolds as a function of its microstructure and fibers properties can help in achieving the aimed specifications for the target application by much more efficient methods. [11, 12]. In this sense, mechanical constitutive modeling of nanofibrous structures appears as a powerful design tool, with the potential to link the fiber properties and scaffold microstructure to the desired macroscopic response [11, 12]. In particular, multiscale mechanical models that represent the nanofibrous network at the microstructure have been studied with different degree of success [4, 5, 11, 12, 18–23]. To represent the electrospun network *in silico*, different Representative Volume Elements (RVEs) with varying levels of complexity were considered. From unit cells with three or four representative fibers [12, 24], to more recently, discrete networks models [2, 4, 11, 18–20, 22, 25]. The ideal RVE should mimic the scaffold microstructure to the highest possible degree, allowing the selection of fiber material, size and arrangement that would result in the desired mechanical properties of the target biological tissue to replace.

In what respects to fibers kinematics, the most common approach consisted in the application of affine deformation [13, 16, 18, 26]; while statistical averaging was also considered [27, 28]. The affine versus non-affine fibril kinematics was discussed for natural extra-cellular collagenous networks [29]. It was found that due to the rearrangement of the fibers during deformation associated with straightening and reorientation mechanisms, a non-affine approach is more representative of the network behavior. Recently, Domaschke et al. [5] presented a predictive computational model based on the geometry and elastic-plastic mechanical properties of single fibers, providing insight to the peculiar kinematics of the fibers, in particular their non-affine motion and realignment.

Different levels of complexity were also used for the nanofibers micromechanical models. From linear mechanical models [18, 30], to the inclusion of fiber breaking [13], and plasticity [12], resulting in a nonlinear macroscopic response. Other studies considered more complex, nonlinear hyperelastic constitutive laws [11, 14, 16, 24], even though the use of such laws does not comply well with reported mechanical tests for individual nanofibers [31–36]. Moreover, experimental observations indicate that initially wavy nanofibers straighten and align along the applied load direction during tensile test [12, 36, 37]. This is a phenomenon that closely resembles the straightening mechanism, usually called recruitment, of natural fibers in collagen

networks, which greatly increase their load bearing capacity when they become straight. This particular mechanism is responsible for the non-linear 'J-shaped' response of most biological tissues where collagen fibers are a relevant component [38, 39].

In a recent work, we introduced a micromechanical model that accounts for the progressive straightening of initially undulated nanofibers (i.e. progressive recruitment) [22]. We emphasized that this process, taking place at the microscale of electrospun scaffolds, contributes to the highly nonlinear macroscopic behavior observed in nanofibrous structures. The use of a multiscale constitutive model helped to understand and explore the most relevant features that result in the characteristic mechanical behavior of nanofibrous scaffolds, providing the explanation of the material constitutive behavior in terms of natural, easily recognizable and measurable parameters.

In this work, a more realistic microscopic element is being considered for the electrospun network as well as a less restrictive approach for the microscopic kinematics, allowing for fiber recruitment, reorientation and interaction. Following the works of Carleton et al. [40] and Zündel et al. [23], we begin by generating an RVE through a virtual deposition algorithm that mimics the electrospinning process itself, thus obtaining geometries that resemble the observed electrospun microstructure. These geometries were then validated by comparison with analysis of SEM images, taking special interest in orientation and tortuosity distributions. Then, an elastic-plastic constitutive law for the nanofibers is implemented along with a simplified kinematic description that allows a significant reduction of the number of degrees of freedom of the associated algebraic system of equations. Finally, the micromechanical model is validated against uniaxial tensile tests of electrospun PLLA bone-shaped samples, successfully reproducing the experimental response while being compliant with reported values for the fibers constitutive parameters.

2. Material and Methods

2.1. Materials

Poly(L-lactic acid) (PLLA) (PLA2002D, Mn $78.02\,\mathrm{kg/mol}$, Mw $129.91\,\mathrm{kg/mol}$, IP 1.67) membranes were produced by the electrospinning technique with methodology and conditions previously optimized by Montini-Ballarin et al. [41]: solution concentration 10% wt/V in dichloromethane (DCM) and dimethylfor-

mamide (DMF) with 60:40 v/v proportion; flow rate $0.5\,\mathrm{ml/h}$, needle-collector distance $10\,\mathrm{cm}$, and applied voltage $10\,\mathrm{kV}$.

The electrospinning setup consisted of a high voltage power supply (Gamma High Voltage Research Inc., Ormond Beach, Florida, USA), a blunt stainless steel needle (18 gauge, Aldrich®), a syringe pump (Activa®A22 ADOX, Ituzaingó, Argentina), and a plane collector of stainless steel. The electrospinning process was carried out for 2 h, while the needle position was shifted every $15\,\mathrm{min}$ to achieve a uniform thickness along the membrane dimensions. Circular specimens of 15-20 cm were produced. Then, a punch was used to die-cut dumbbell-shaped specimens from the membranes (Fig. 1). Additionally, some samples were separated to obtain SEM images in order to characterize the electrospun microstructure.

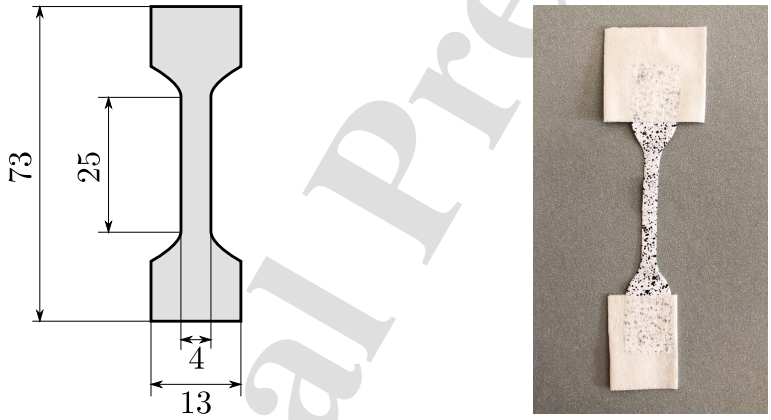

(a) (b)

Figure 1: a) Dimensions of the PLLA dumbbell specimens (in mm). Thickness values were measured at several points for each specimen, with values between $0.05\,\mathrm{mm}$ and $0.07\,\mathrm{mm}$. b) Image of a specimen ready to be tested (a speckle pattern was applied in order to apply Digital Image Correlation techniques).

2.2. Scanning Electron Microscopy (SEM)

Electrospun samples were sputter-coated with a thin layer of gold to perform Scanning Electron Microscopy (SEM) (JEOL Model JSM-6460LV). SEM images of the samples were taken and imported into ImagePro Plus software (Media Cybernetics Inc., USA) for analysis of the microstructure geometry (Fig. 2). The fiber orientation and tortuosity of 100 fibers was analyzed for each sample. The tortuosity of a fiber is defined as the ratio of its contour length to its end-to-end length. The orientation for non straight fibers was measured along the end-to-end line.

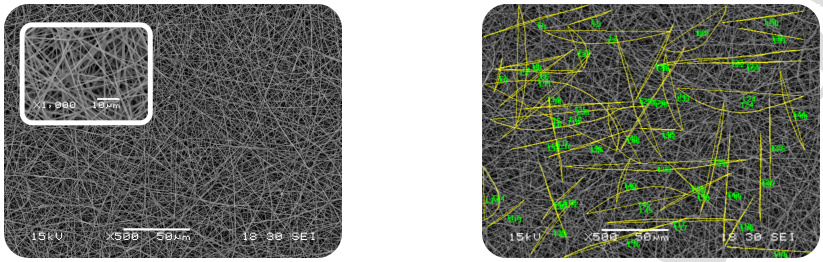

(a) (b)

Figure 2: Microstructure characterization from SEM analysis of PLLA electrospun scaffolds.

2.3. Mechanical Testing

Uniaxial tensile tests were conducted on the electrospun dumbbell-shaped specimens. The thickness of each specimen was determined from the average of three measurements with an absolute digital caliper 573-191-20 (Mitutoyo, Japan). These values fall in the range 0.05-$0.07\,\mathrm{mm}$ depending on the region of the membrane from which the specimen is taken.

The samples were pulled monotonically at a rate of $6\,\mathrm{mm/min}$ on an Instron EMIC 23-50 universal tensile testing system. Video extensometry was employed to monitor both axial and transverse strain. To that end, the specimens were covered with a speckled pattern (Fig. 1b) and the images were recorded and post-processed with the Vic2d system from Correlated Solutions (Fig. 3a) [42]. Knowing the zone in the specimen where the failure took place, allowed for an accurate measurement of the strain at this area (Fig. 3b). Elastic modulus, yield stress and post-yield tangent modulus were measured from the stress-strain curve. Results are presented as mean $\pm$ standard deviation for $N = 3$ samples.

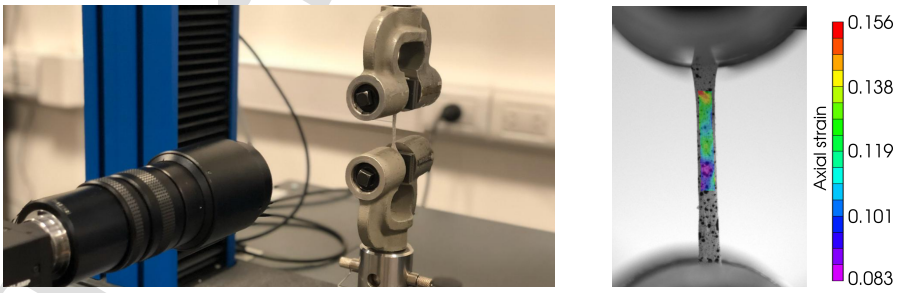

(a) (b)

Figure 3: Setting for the uniaxial tensile tests showing the camera lens (left) and a processed showing a color map according to the axial strain (right).

3. Calculation

3.1. Formulation of the model

3.1.1. Generation of Representative Volume Elements (RVE)

A virtual deposition algorithm is developed to generate geometries that resemble the microstructure of electrospun structures according to SEM observations. This algorithm closely follows the works of Zündel et al. [23] and Carleton et al. [40], with an improvement in the required parameters to employ variables with experimental meaning and feasible to measure.

The generated geometry is a superposition of N_l plane layers, where each layer is virtually deposited with a methodology that imitates the real deposition of nanofibers during the electrospinning process. Within each layer, the nanofibers are approximated as piece-wise linear curves consisting of a concatenation of straight segments.

The algorithm steps for the deposition of a single fiber are as follows (see also Fig. 4):

Algorithm: Deposition of a single fiber

1. Set a square domain of side length L_μ
2. Randomly select a point $\mathcal{P}_1$ on the border
3. Deposit the first segment, of length l_s and angle θ_1. This angle can be generated from an orientation distribution function that must be defined beforehand
4. Concatenate a second linear segment, of same length l_s, but with with an angle θ_2 which deviates from θ_1 by a value ${\theta^d}_2$. The deviation angle is randomly selected from the interval $\left[-{\theta^d}_{max}, +{\theta^d}_{max}\right]$, where ${\theta^d}_{max}$ is the maximum deviation angle between segments
5. Repeat this concatenation of linear segments until the fiber curve exits the layer domain, at which point the last segment is trimmed

The deposition of fibers within the layer is repeated until a desired volume fraction (η) is achieved. The volume fraction (i.e. the ratio of volume occupied by the fibers to the total volume of the layer) is calculated considering that the layer thickness is equal to the fibers diameter D. Additionally, it is noted that the volume fraction (η) may be related to porosity (p) of the mesh by the relationship p = 1 (η).

Finally, the intersections between the fibers are computed, restricting the possibility of contact between fibers within the same layer and adjacent layers (Fig. 5). This approach also allows to estimate the cross-link density (δ), a microstructural parameter that is particularly difficult to measure experimentally [43, 44] and, at the same time, essential for a reliable prediction of the macroscopic behavior [23].

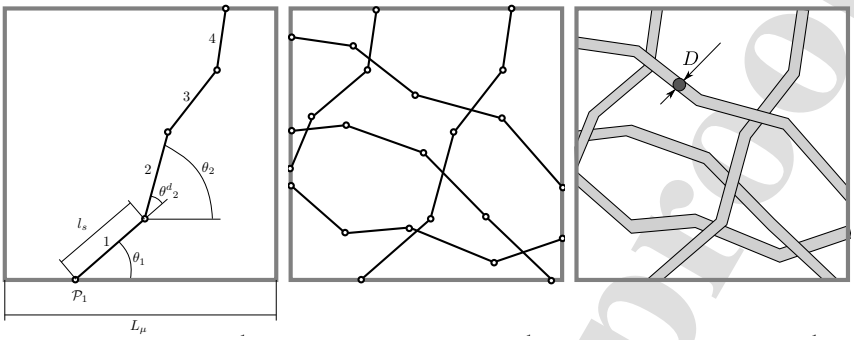

Figure 4: Virtual deposition of a layer of fibers. a) Each single fiber is virtually deposited starting at a random boundary point and then concatenating linear segments until the fiber exits the RVE. b) The same process is repeated thus obtaining several fibers with different orientations and tortuosity. c) The process ends when the volume occupied by the fibers reaches a prescribed fraction of the total RVE volume. To compute the volume of the fibers, their diameter D must be supplied beforehand.

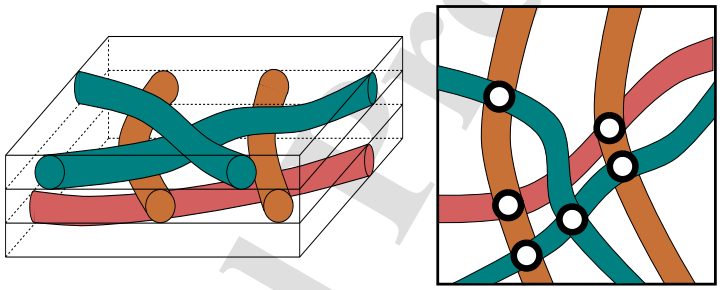

Figure 5: Cross-links (white circles) between fibers occur only within the same layer or between fibers from adjacent layers. In this schematic example, there is an apparent intersection between the red and green fibers (as seen in the projection at the right), but their corresponding layers are too far apart in the out-of-plane coordinate, and therefore no cross-link is generated.

It is also possible, and convenient, to formulate the algorithm in terms of dimensionless lengths, using D as the normalizing scale length, and defining $\tilde{L_\mu} = \frac{L_\mu}{D}$ as the dimensionless layer length, and $\tilde{l_s}$ as the dimensionless segment length.

3.1.2. Determination of RVE size

Given the stochastic nature of the virtual deposition algorithm, the obtained geometries exhibit statistical differences between each other. This difference naturally decreases for meshes with a greater population of fibers, with in turn depends upon the mesh size. The size of a virtual mesh, defined by both $\tilde{L_\mu}$ and N_l, must be large enough to properly represent the overall properties of the material at a given macroscopic point. This means that set of geometries of the same size should have essentially the same orientation and

tortuosity distributions, as well as the same intersection density.

To determine the necessary size of the meshes to qualify as RVEs, we conducted a study of the statistical variation of these geometric properties versus mesh size, presented in detail in Appendix A.

3.1.3. Fiber Mechanical Model

To establish a mechanical model for the proposed RVE, first we must describe the mechanics of its constituents: the electrospun nanofibers. The fibers in the mesh are in reality three-dimensional bodies. However, due to their long and slender shape, a 3-D continuum model approach becomes impractical. As a result, the usual approach to the kinematics of fiber meshes implies the idealization of each fiber as a one-dimensional structural element that exists in a 3-D space [4, 11, 23]. In this work, we propose an additional simplification to the fiber kinematics by acknowledging that although electrospun fibers are stiff under traction, their flexural resistance is negligible, causing them to easily buckle up under compression [45, 46]. Therefore, in our model, the elastic behavior of the fiber resembles a bilinear spring characterized by a taut and a slack elastic modulus (E_t and E_b respectively), depending if the fiber is straight or kinked, as shown in Fig. 6 [22].

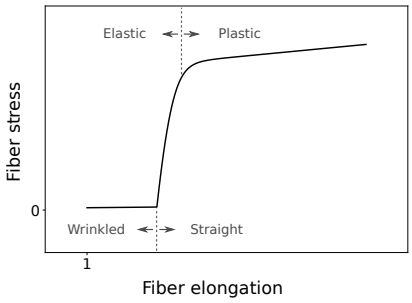

Figure 6: Mechanical behavior of a single fiber under traction: in its initial configuration the fiber is wrinkled and exhibits a very small resistance against deformation. Once it becomes straight, its stiffness increases significantly. Then, at larger elongations, the fiber reaches a yield threshold stress, followed by a linear plastic response. Although at some point the fiber would break, that region of the curve was intentionally left out, because such phenomena was not taken into consideration in the present model.

The main advantage of this approach is a significant reduction of the number of Degrees of Freedom (DOF) needed to describe the kinematics of each nanofiber. With the usual approach where each fiber is modeled as a beam, the position and rotation values of every point in the 1D representation of the fiber must be acknowledged for, whereas with the proposed representation only the positions of its two extreme points

are needed.

In addition, it can be stated that an initially wrinkled fiber under traction shows negligible resistance up to the point when it becomes straight (i.e. gets recruited), greatly increasing its load bearing capacity thereafter. More important, in a previous work we observed that the progressive recruitment of the fibers is a crucial factor for the non-linearity in the mechanical response under traction of nanofibrous meshes [22]. In such cases, the subset of fibers that are straight (recruited) bear the vast majority of the applied load, while the contribution of the wrinkled fibers is merely marginal.

To describe an individual fiber within the mesh according to the previous concepts, we will define two quantities: an orientation unit vector ($\mathbf{a}$) aligned with the end-to-end line of the fiber, and the initial tortuosity of the fiber (λ_0^r) defined as the ratio of its initial contour length (L_0) to its initial end-to-end length (l_0) [22]. The initial tortuosity of the fiber is a crucial parameter, greatly affecting the fiber mechanical behavior, because it defines wether the fiber is wrinkled ($\lambda_0^r > 1$) or straight ($\lambda_0^r = 1$) in the initial configuration. Under this simplified description, it results a practical approach to introduce the end-to-end elongation of the fiber (λ), defined as the ratio of end-to-end length to resting end-to-end length (l_0): $\lambda = l/l_0$ (Fig. 7).

Then, from the provided definitions for λ and λ_0^r, it follows that the fiber gets recruited at the deformation given by $\lambda = \lambda_0^r$, meaning that the initial tortuosity coincides with the recruitment end-to-end elongation of the fiber. This same approach has been successfully applied for polymeric networks in the context of constitutive models for rubber materials under large deformations [47].

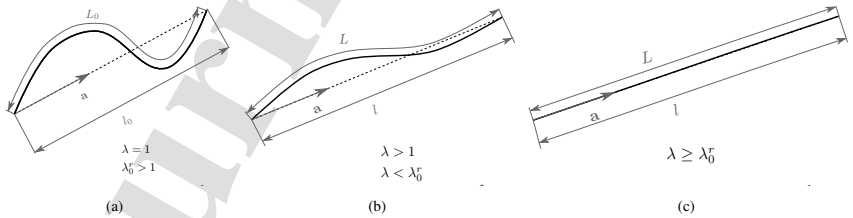

Figure 7: Reduced kinematic description of a fiber: a) in its initial configuration the fiber is wrinkled, b) the fiber is somewhat deformed but remains wrinkled, c) the fiber is deformed and has become straight. The initial end-to-end length (l_0) is selected as the reference length to measure the fiber elongation ($\lambda = l/l_0$). The initial tortuosity of the fiber ($\lambda_0^r = L_0/l_0$) measures how far from becoming straight the fiber is in its initial configuration.

Observe that, according to given description, $\lambda = 1$ corresponds to the fiber in its initial, wrinkled, configuration. Then, as the ends of the fiber are pulled further apart ($\lambda > 1$) it gradually uncurls, but still

remaining wrinkled while $\lambda < \lambda_0^r$, therefore offering a small resistance to deformation, represented by the small elastic modulus E_b. With further elongation the fiber eventually becomes straight (i.e., gets recruited) at $\lambda = \lambda_0^r$, greatly increasing its resistance to deformation, thus shifting its elastic modulus to the much bigger E_t. Consequently, the elastic response of the fiber is given by the following stress vs elongation equation:

$$t = \begin{cases} E_b\left(\lambda - 1\right) & if \quad \lambda < \lambda_0^r \\ E_b\left(\lambda_0^r - 1\right) + E_t\left(\dfrac{\lambda}{\lambda_0^r} - 1\right) & if \quad \lambda \geq \lambda_0^r \end{cases} \tag{1}$$

Where the constitutive equation for a nanofiber is defined in terms of engineering stress (1st Piola Kirchoff stress), that is, force per unit area of the reference section. In this way, there is the advantage of being able to directly correlate the stress-strain curve with data from experimental measurements.

To introduce plastic behavior into the model, we assume a simple law where the same plastic elongation (λ^p) is applied equally to both the initial resting contour length (L_0) and the initial resting end-to-end length (l_0):

$$L_0' = \lambda^p L_0 \tag{2}$$

$$l_0' = \lambda^p l_0 \tag{3}$$

where L_0' and l_0' are the resting contour length and resting end-to-end length of the fiber after suffering plastic deformation.

To obtain λ^p, we employ a constitutive equation for the rate of plastic elongation ($\dot{\lambda^p}$) depending upon the axial stress [12]:

$$\dot{\lambda^p} = a_p \sinh\left(\frac{t}{b_p\left(\lambda^p\right)^{c_p}}\right) \tag{4}$$

where a_p is a proportionality coefficient measured in $\left[\mathrm{s}^{-1}\right]$, b_p is the initial resistance to yield with units of stress, and c_p is the post-yield hardening exponent.

Then, the proposed elastic-plastic constitutive law can be summarized in the following equation:

$$t = \begin{cases} E_b \left(\dfrac{\lambda}{\lambda^p} - 1 \right) & if \quad \lambda < \lambda^p \\ E_b \left(\lambda_0^r - 1 \right) + E_t \left(\dfrac{\lambda}{\lambda_0^r \lambda^p} - 1 \right) & if \quad \lambda \geq \lambda_0^r \lambda^p \end{cases} \tag{5}$$

3.1.4. Mesh Equilibrium

The idealized microscale consists in a mesh of fibers inter-connected at their end nodes (Fig. 8). The constitutive elements of this mesh are the set of fibers ($\mathcal{F}$) and the set of nodes ($\mathcal{N}$). The nodes can be further subdivided between the set of inner nodes ($\mathcal{N}_I$) and the set of boundary nodes ($\mathcal{N}_B$). Note that $\mathcal{N}_I \cup \mathcal{N}_B = \mathcal{N}$ and $\mathcal{N}_I \cap \mathcal{N}_B = \emptyset$, where $\emptyset$ is the null set. To work with these sets, we employ an enumeration:

$$\mathcal{N} = \{n;\ n = 1,\ ...,\ N_n\} \tag{6}$$

$$\mathcal{F} = \{i;\ j = 1,\ ...,\ N_f\} \tag{7}$$

where N_n is the total number of nodes and N_f the total number of fibers in the mesh.

Additionally, since every fiber spans between two nodes, we can also express it as an ordered pair:

$$\mathcal{F} = \{i \mapsto (i_1, i_2);\ i_1 \in \mathcal{N};\ i_2 \in \mathcal{N};\ i = 1,\ ...,\ N_f\} \tag{8}$$

where i_1 and i_2 are the initial node and the end node of the fiber, respectively.

Inversely, each node n is connected to the subset of fibers $\mathcal{F}_n$ that either has n as their initial node or

end node:

$$\mathcal{F}_n = \{i \mapsto (i_1, i_2)\,;\; i_1 \in \mathcal{N};\; i_2 \in \mathcal{N};\; i = 1,\; ...,\; N_f;\; n \in (i_1, i_2)\} \tag{9}$$

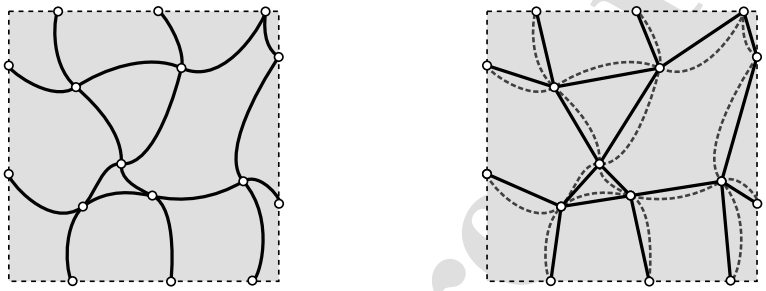

(a) (b)

Figure 8: Mesh schematic showing the reduced kinematic description of the fibers. a) The fibers as virtually deposited form piece-wise linear curves that can intersect each other forming cross-links. b) In the simplified kinematic description, each fiber is reduced to its end-to-end line plus a parameter (its initial tortuosity).

Observe that the deformation of the mesh is completely defined by the nodes displacements, because they determine the fibers elongations. For the node n, we can write its displacement $\mathbf{u}_n$ as:

$$\mathbf{u}_n = x_n - X_n \tag{10}$$

where x_n and X_n are the current and initial positions of the node n, respectively.

It is important to note that, while the displacement of the inner nodes will result from the equilibrium of the mesh, the displacement of the boundary nodes is prescribed following an homogeneous deformation according to the macroscopic deformation gradient tensor $\mathbf{F}$:

$$\mathbf{u}_n = (\mathbf{F} - \mathbf{I})\, X_n \quad \forall n \in \mathcal{N}_B \tag{11}$$

To calculate the force exerted by a fiber i to a node n ($\mathbf{f}_i^n$), we define a fiber-node orientation vector $\mathbf{a}_i^n$

such that:

$$\mathbf{a}_i^n = \begin{cases} \mathbf{a}_i \quad if \quad n = i_1 \\ - \quad \mathbf{a}_i \quad if \quad n = i_2 \end{cases} \tag{12}$$

where $\mathbf{a}_i$ is the orientation vector for the fiber i defined from its initial node (i_1) to its end node (i_2).

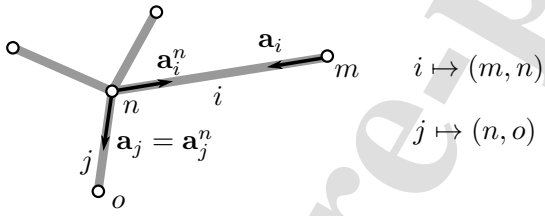

Figure 9: Node n and the fibers connected to it (represented by their end-to-end lines), of which two have their numeration shown as i and j. The fiber i connects the node n to the node m, and the fiber j connects it to the node o. Since the node n is the final node of the fiber i ($i_2 = n$), then its orientation vector $\mathbf{a}_i$ points towards n, and therefore $\mathbf{a}_i^n = -\mathbf{a}_i$. For the fiber j the case is different because its orientation vector ($\mathbf{a}_j$) already points outwards from n, resulting in $\mathbf{a}_j^n = \mathbf{a}_j$.

At a given configuration, the deformation of the fiber i depends on the initial and end positions of its end nodes:

$$\lambda_i = \frac{||x_{i_2} - x_{i_1}||}{||X_{i_2} - X_{i_1}||} \tag{13}$$

Then, $\mathbf{f}_i^n$ can be expressed as:

$$\mathbf{f}_i^n = t_i \frac{\pi D_i^2}{4} \mathbf{a}_i^n \tag{14}$$

Finally, to calculate the equilibrium of the mesh, we postulate that the sum of forces exerted by the

fibers at each inner node must be zero:

$$\sum_{i \in \mathcal{F}_n} \mathbf{f}_i^n = \mathbf{0} \qquad \forall n \in \mathcal{N}_I \tag{15}$$

3.1.5. Stress homogenization

Once the equilibrium configuration of the mesh is found, the macroscopic Cauchy stress tensor ($\mathbf{T}$) is obtained as the average of its microscopic counterpart ($\mathbf{T}_\mu$) over the volume of the RVE (V_μ):

$$\mathbf{T} = \frac{1}{V_\mu} \int_{V_\mu} \mathbf{T}_\mu \mathrm{d}V_\mu \tag{16}$$

For the present case, however, it is convenient to express this as a sum over the volumes of the fibers:

$$\mathbf{T} = \frac{1}{V_\mu} \sum_{i \in \mathcal{F}} \left[t_i \left(\mathbf{a}_i \otimes \mathbf{a}_i \right) V_i \right] \tag{17}$$

where $t_i \left(\mathbf{a}_i \otimes \mathbf{a}_i \right)$ is the microscopic Cauchy stress tensor, and V_i is the volume of the fiber i, considered to be incompressible.

In the expression above it is assumed that the stress tensor within each fiber is constant and the fiber only undergoes traction along its orientation line. Observe that, as a consequence of the selected constitutive equation for individual fibers, the contribution of wrinkled fibers to the overall macroscopic stress is only marginal, and therefore we can apply the proposed formula without introducing any significant error to the homogenized response.

4. Results and Discussion

4.1. Experimental Results

The processing of SEM images with Image-Pro Plus software allowed to characterize the electrospun PLLA microstructure, obtaining orientation, diameter, and tortuosity histograms (Fig. 2). The orientation distribution corresponds to an isotropic arrangement with no preferred alignment, assumed to be product of a uniform probability density function (PDF) (Fig. 10a). The diameter measurements show a unimodal distribution that can be accurately represented by a Normal PDF with mean $0.463\,\mu\mathrm{m}$ and standard deviation $0.131\,\mu\mathrm{m}$ (Fig. 10b). The tortuosity distribution, however, exhibits a positive asymmetric distribution as a consequence of the geometric condition of $\lambda^r > 1$ (see section 3.1.3). A good representation of this histogram can be obtained by a Truncated Normal PDF with a mean of 1, a standard deviation of 0.14, and a minimum tortuosity value of also 1 (being thus equivalent to a half of a Normal PDF, renormalized) (Fig. 10c).

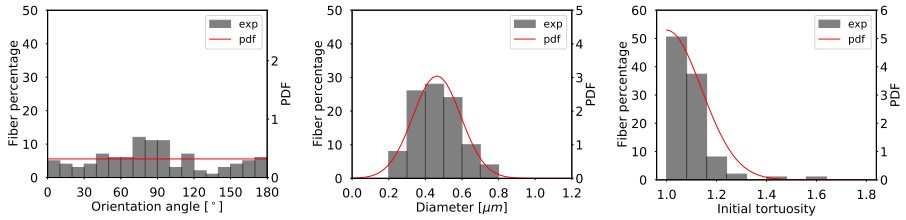

(a) (b) (c)

Figure 10: Characterization of the electrospun PLLA microstructure from analysis of SEM images. a) The fiber orientation angle histogram shows an isotropic distribution that can be represented by a uniform PDF . b) Diameter histogram showing a unimodal distribution that can be represented by a Normal PDF (mean is $0.463\,\mu\mathrm{m}$ and standard deviation is $0.131\,\mu\mathrm{m}$). c) Initial tortuosity histogram showing a positive asymmetric distribution that can be represented by a Truncated Normal PDF (mean is 1, standard deviation is 0.14, and minimum tortuosity value is 1.

The uniaxial tensile stress-strain response was found to be elastic-plastic with some degree of post-yield hardening (Fig. 11). The samples show an initial linear elastic response up to a strain of 0.03. This behavior is followed by a yield event and an almost linear plastic response until failure. It was also observed that necking occurred previous to failure. This can be related to the material microstructure, because during uniaxial traction, the reorientation of fibers along the load direction at the area of the sample where the strain is maximum generates an additional transverse contraction that evolves into necking. The results for the elastic modulus, yield stress and post-yield modulus are summarized in Table 1.

Table 1: Mechanical properties of the tested PLLA electrospun samples, calculated from the uniaxial stress-strain curves.

	#1	#2	#3	Avg.	Std.Dev.
Elastic modulus (MPa)	76.74	105.56	127.20	103.17	20.67
Yield stress (MPa)	1.46	1.33	1.47	1.42	0.061
Post-yield modulus (MPa)	6.92	5.63	6.08	6.21	0.54

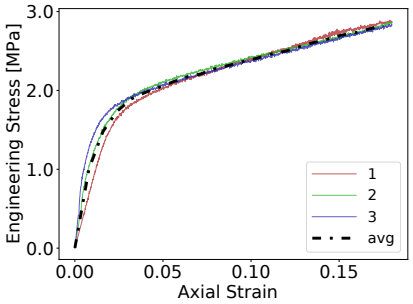

Figure 11: Uniaxial tensile characterization of electrospun PLLA. The three obtained stress-strain curves are shown together with the average curve.

4.2. Comparison with Experimental Measurements

The parameters of the virtual deposition algorithm were optimized to obtain geometries that resemble the analyzed electrospun PLLA microstructure (Table 2. To this end, the orientation of the virtual fibers is drawn from a uniform distribution successfully obtaining geometries with no preferred alignment (Fig. 12b). The virtual tortuosity histogram, controlled through $\tilde{l_s}$ and ${\theta^d}_{max}$, has a positive skew distribution similar to the experimental histogram, but with some difference in the standard deviation, being greater for the virtual histogram. The main difference was the choice of a fixed diameter value of $0.45\,\mu\mathrm{m}$ for all the virtual fibers instead of admitting a statistical distribution. The volume fraction, on the other hand, was optimized to fit the macroscopic stress-strain response of the uniaxial tensile tests (obtaining $\eta = 0.19$) that complies well with reported experimental estimations [48].

Table 2: Parameters of the virtual deposition algorithm used to generate geometries similar to the electrospun microstructure.

$D[\mu\mathrm{m}]$	η	$\tilde{L_\mu}$	$\tilde{l_s}$	${\theta^d}_{max}$	N_l	p^θ
0.45	0.19	200	5	5°	15	π^{-1}

The taut elastic modulus for the virtual fibers, E_t, was set to $3.0\,\mathrm{GPa}$ as reported by others for PLLA nanofibers [49]. The value of E_b, although necessary to avoid displacement indeterminacies of the nodes

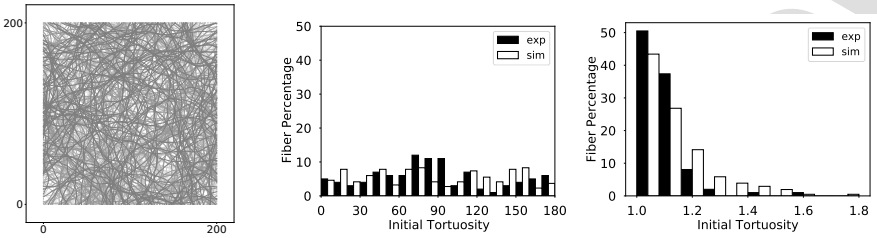

(a) (b) (c)

Figure 12: Comparison of the RVE geometry to the electrospun microstructure. a) Virtual deposited geometry generated with the parameters given in table 2. b) Orientation histogram for the simulated mesh together with the experimental result obtained from SEM images. c) Initial tortuosity histogram for the simulated mesh, also shown together with the experimental histogram.

connected to wrinkled fibers, has only a negligible effect upon the overall response and does not affect the resulting stress-strain curve. It is therefore set to one thousandth of E_t (3.0 MPa). The rest of the constitutive parameters were optimized to fit the average experimental stress-strain curve (Table 3). The resultant fit is shown in Figure 13 along with the virtual fiber response corresponding to the optimized constitutive parameters.

It is interesting to observe that the experimental stress-strain response was reproduced employing an RVE that emulates the real microstructure according to the SEM image analysis. Simultaneously, the modeled single fiber response agrees well with the experimental behavior reported by others for single PLLA nanofibers [31, 49]. This represents a new step forward in the modeling of nanofibrous materials, since many previous similar models rely on the introduction of non realistic features such as the presence of a base continuous material, the assumption of non-linear hyperelastic fiber response, or the imposition of a periodic geometry, among others [11, 12, 23].

Table 3: Constitutive parameters optimized to adjust the experimental stress-strain response.

E_t[MPa]	E_b[MPa]	a_p[1/s]	b_p[MPa]	c_p
3.0×10^3	3.0	1×10^{-8}	5.0	0.5

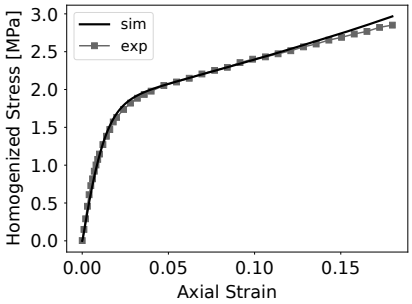

Figure 13: Uniaxial tensile response of the RVE fitted to reproduce the experimental data. The obtained fit was very good ($R^2 = 0.994$), specially for the low and mid range of deformations where its most important, since the higher deformations would fall outside of the working range for biomimetic scaffolds.

4.3. DOF Analysis

The use of computational simulations to help guide the experimental design of electrospun scaffolds is a helpful approach, and it has been widely explored in several works [9, 18, 19, 21, 22, 28, 50]. The objective of this development is the *in silico* design of tailored microstructures for patient-specific scaffolds that can be effectively realized. To achieve such a goal, a candidate model must be integrated into an optimization algorithm in order to obtain the parameters that define a microstructure that meets the design requirements. It is important to note that, as a result of the optimization stage, the computational efficiency of the simulations becomes an important feature. However, the usual approach for fibrous networks simulations based on RVEs, where fibers are modeled as slender beams (discretized in finite elements), entail a high computational cost [4, 5, 11, 23].

Here we present a reduced kinematic description for the fibers in the network (see section 3.1.3) that leads to a significant reduction of the number of DOF, compared with recent efforts where the RVEs consider slender beams models for the fibers (Fig. 14) [23]. Therefore, while avoiding costly finite element models for each individual fiber of the mesh, the proposed approach is still composed by an RVE that resembles the electrospun microstructure, preserving a detailed representation of the fibrous network as a whole, and thus achieving a balance between performance and accuracy. As a consequence, the model is formulated in terms of observable and meaningful parameters, allowing for an effective communication between simulations and experimentation. Simultaneously, its reduced kinematics are an advantage for optimization applications where computational efficiency becomes crucial.

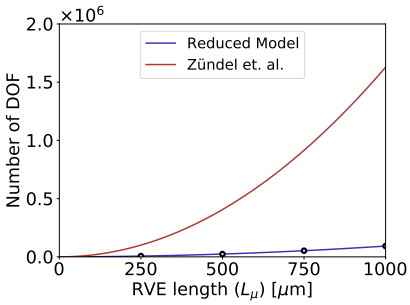

Figure 14: Number of Degrees of Freedom (DOF) versus RVE size for the proposed model with the reduced kinematic fiber description, compared with the values reported by Zündel et al. [23] for a finite element fiber network model. The results show a reduction in the number of DOF by over a factor of 10. To make a valid comparison, for each RVE size a number of $N = 10$ meshes were generated following the parameters given in [23]. The mean number of DOF for each size was calculated and plotted (circles) while the standard deviation was found to be negligible. A quadratic regression is also shown (blue line).

Naturally, the reduced kinematic approach does not capture the positions of all the points that conform the fibers as a 1D curves within the RVE. As a consequence, the interactions between nanofibers are assumed to occur only at cross-links in which the displacements are linked. Other types of interaction due to contact and friction, that can take place during the deformation of the RVE, are disregarded. The inclusion of contact forces between fibers, however, is expected to become a relevant phenomena only if nanofibers become densely packed. In the case of uniaxial traction, for instance, this could happen at large deformations due to the lateral contraction, where fibers become highly aligned and approach one another within each layer. Nonetheless, such deformations would fall outside of the typical range of interest for biomimetic applications, which is the intended aim.

5. Conclusions

In this work, we presented a micromechanical model for electrospun scaffolds taking into account the main aspects of the nanofibrous microstructure. The proposed RVE is constructed following a virtual deposition algorithm inspired in the electrospinning process itself, obtaining geometries highly correlated with actual features of the electrospun microstructure according to SEM image analysis. This algorithm assumes that the fibers are deposited according to a set of parameters that stochastically determine their position, orientation and tortuosity. Finally, cross-links are introduced where fiber intersections occur.

A simplified kinematic representation was adopted for the fibers, where the end nodes positions and

initial tortuosity fully describe the deformed configuration, thus greatly reducing the total number of degrees of freedom in the micromechanical model. The elastic mechanical behavior of the fibers was modeled with a simple bilinear law defined by a taut and a slack elastic modulus depending on the fiber state being straight or wrinkled, respectively. Plastic behavior was also considered with the introduction of a yield stress and post-yield hardening.

The use of a micromechanical model contributed to explore and understand the most relevant features that result in the typical mechanical behavior of nanofibrous materials, providing a way to explain the complex material macroscopic behavior relying on simple microscopic phenomena.

To validate the model, microscopic characterization via SEM and uniaxial tensile tests were performed on PLLA electrospun samples. Analysis of the SEM images using image processing software allowed to obtain the experimental diameter, orientation and tortuosity distributions. The uniaxial stress-strain curves exhibited an elastic-plastic macroscopic behavior, from which elastic modulus, yield-stress and post-yield modulus were extracted. Then, the virtual deposition algorithm parameters and constitutive parameters were either imposed to reported values or adjusted to fit both the observed microstructure and the experimental uniaxial curves. Most importantly, the values of the adjusted parameters fall within expected ranges according to experimental works, meaning that the overall mechanical response was successfully reproduced while maintaining a good representation of the microscopic mechanical behavior. Even more, they could be set as a function of microstructure measurements and individual fiber properties. Consequently, the proposed model could be used to predict the macroscopic mechanical response of electrospun networks.

Finally, the presented RVE can be a good candidate to be included in multiscale frameworks for mechanical analysis, having the advantage of a reduced number of Degrees of Freedom while maintaining a faithful representation of the material behavior.

6. Acknowledgment

This research work was partly funded by CONICET (Consejo Nacional de Investigaciones Científicas y Técnicas de la República Argentina), and by Agencia Nacional de Promoción Científica y Tecnológica (Argentina), Grant PICT 0302/16 and Grant PICT 00543/18.

Appendix A. Determination of RVE size

The stochastic nature of the virtual deposition algorithm means that meshes generated employing the same set of parameters will differ from one another. Still, it is expected that for sufficiently large meshes, the statistical variation will become negligible. Therefore, in order to determine the minimal RVE size that yields statistical equivalent geometries, the mean and standard deviation of the mechanical properties (elastic modulus, yield stress and post-yield modulus) is computed for a set of $N = 10$ meshes generated under the same set of deposition parameters. Additionally, to obtain results independent from scaling effects, instead of the length L_μ for the RVE size, the length $\tilde{L_\mu}$ normalized by the mean fiber diameter is used as independent variable.

The obtained mechanical parameters are plotted against RVE size (both $\tilde{L_\mu}$ and N_l), showing that they converge to stable values for increased RVE sizes, as the standard deviation decreases. This proves to be equally true for the three analyzed mechanical parameters: the elastic modulus (Fig. A.15), the yield-stress (Fig. A.16), and the post-yield modulus (Fig. A.17). To better quantify this phenomena, we also compute the Relative Standard Deviation (RSD), defined as the ratio between the standard deviation and the mean, for each property and each RVE size. Although there is no established threshold to achieve, we show that with $\tilde{L_\mu} = 200$ and $N_l = 15$ the RSD falls below 2% for the three analyzed parameters. Furthermore, in that case the mechanical response results in stress-strain curves with little variability (Fig. A.18).

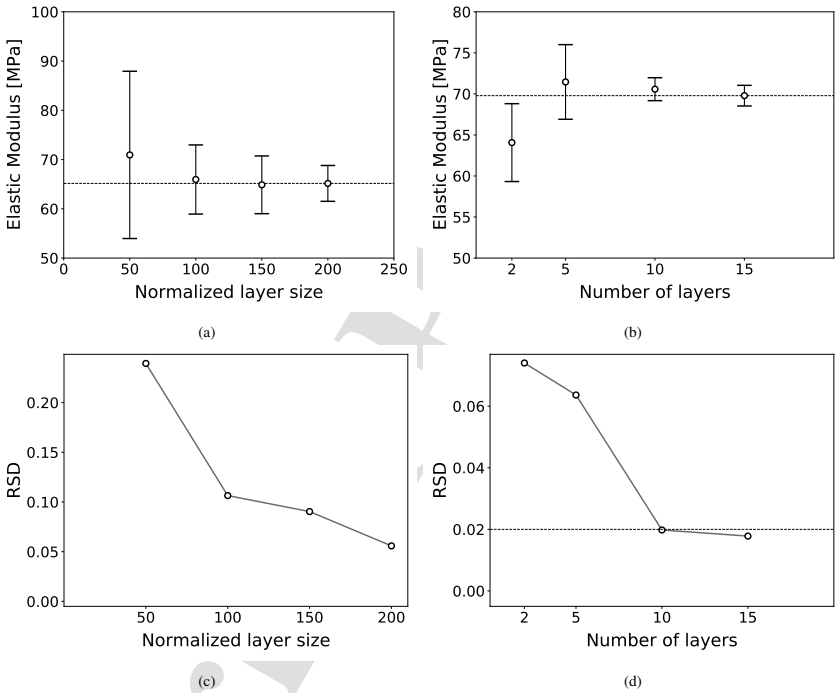

Figure A.15: Statistical variation of the elastic modulus versus RVE size. a) Mean and standard deviation (error-bars) versus layer normalized length $\tilde{L_\mu}$ for meshes consisting of $N_l = 5$ layers. b) Idem for meshes of $\tilde{L_\mu} = 200$ but different N_l. c) RSD corresponding with (a). d) RSD corresponding with (b).

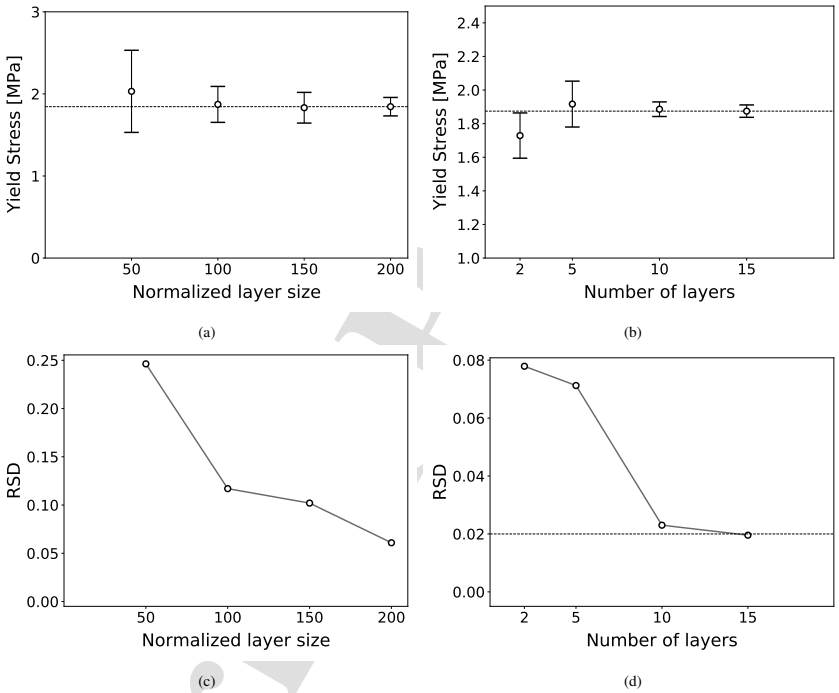

Figure A.16: Statistical variation of the yield stress versus RVE size. a) Mean and standard deviation (error-bars) versus layer normalized length $\tilde{L_\mu}$ for meshes consisting of $N_l = 5$ layers. b) Idem for meshes of $\tilde{L_\mu} = 200$ but different N_l. c) RSD corresponding with (a). d) RSD (b).

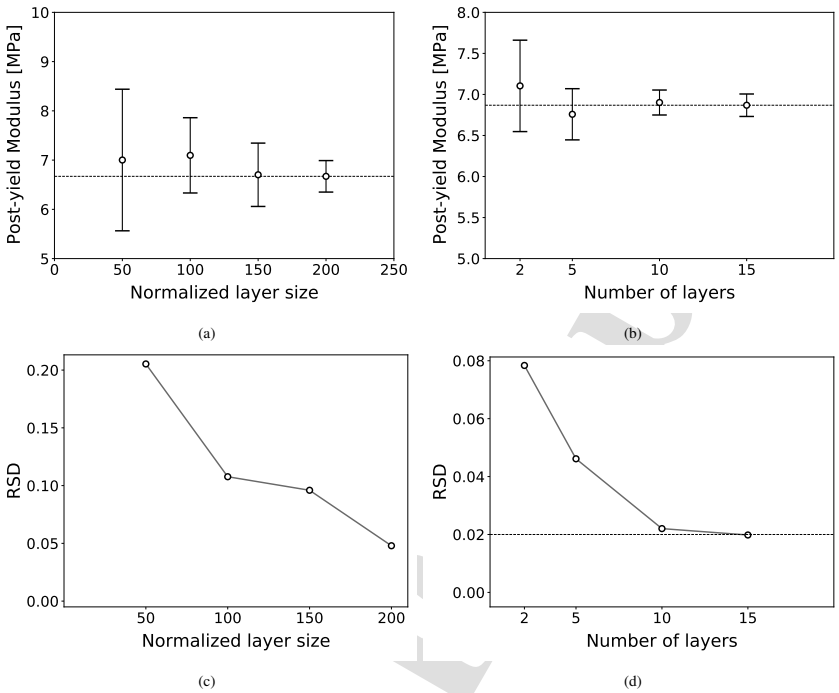

Figure A.17: Statistical variation of the post-yield modulus versus RVE size. a) Mean and standard deviation (error-bars) versus layer normalized length $\tilde{L_\mu}$ for meshes consisting of $N_l = 5$ layers. b) Idem for meshes of $\tilde{L_\mu} = 200$ but different N_l. c) RSD corresponding with (a). d) RSD corresponding with (b).

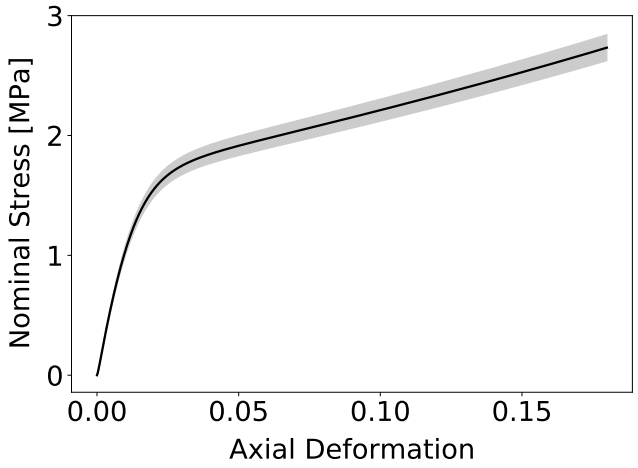

Figure A.18: Statistical variation of the stress-strain curve for $N = 10$ meshes of RVE size given by $\tilde{L_\mu} = 200$ and $N_l = 15$, employing the same parameters used to fit the experimental data in Fig. 13. The plot represents the mean (solid line) and standard deviation (shaded area).

References

[1] S. Thenmozhi, N. Dharmaraj, K. Kadirvelu, H. Y. Kim, Electrospun nanofibers: New generation materials for advanced applications, Materials Science and Engineering B: Solid-State Materials for Advanced Technology 217 (2017) 36–48. doi:10.1016/j.mseb.2017.01.001.

[2] Y. Liu, Y. Dzenis, Explicit 3D finite-element model of continuous nanofibre networks, Micro & Nano Letters 11 (2016) 727–730. doi:10.1016/j.partic.2016.09.003.

[3] A. Arinstein, Supermolecular structure formation during electrospinning, and its effect on electrospun polymer nanofiber unique features, in: Problems of Nonlinear Mechanics and Physics of Materials, Springer, 2019, pp. 173–204. doi:10.1007/978-3-319-92234-8_11.

[4] S. Domaschke, M. Zündel, E. Mazza, A. E. Ehret, A 3d computational model of electrospun networks and its application to inform a reduced modelling approach, International Journal of Solids and Structures 158 (2019) 76 – 89. doi:10.1016/j.ijsolstr.2018.08.030.

[5] S. Domaschke, A. Morel, R. Kaufmann, J. Hofmann, R. M. Rossi, E. Mazza, G. Fortunato, A. E. Ehret, Predicting the macroscopic response of electrospun membranes based on microstructure and single fibre properties, Journal of the Mechanical Behavior of Biomedical Materials 104 (2020) 103634. doi:10.1016/j.jmbbm.2020.103634.

[6] Kenry, C. T. Lim, Nanofiber technology: current status and emerging developments, Progress in Polymer Science 70 (2017) 1–17. doi:10.1016/j.progpolymsci.2017.03.002.

[7] S. Nemati, S.-j. Kim, Y. M. Shin, H. Shin, Current progress in application of polymeric nanofibers to tissue engineering, Nano convergence 6 (2019) 1–16. doi:10.1186/s40580-019-0209-y.

[8] W. M. Abbott, J. Megerman, J. E. Hasson, G. L'Italien, D. F. Warnock, Effect of compliance mismatch on vascular graft patency, Journal of Vascular Surgery 5 (1987) 376–382. doi:10.1016/0741-5214(87)90148-0.

[9] E. Mazza, A. E. Ehret, Mechanical biocompatibility of highly deformable biomedical materials, Journal of the Mechanical Behavior of Biomedical Materials 48 (2015) 100–124. doi:10.1016/j.jmbbm.2015.03.023.

[10] R. M. Nerem, Role of mechanics in vascular tissue engineering, Biorheology 40 (2003) 281–287.

[11] J. B. Carleton, G. J. Rodin, M. S. Sacks, Layered elastomeric fibrous scaffolds: An in-silico study of the achievable range of mechanical behaviors, ACS Biomaterials Science and Engineering 3 (2017) 2907–2921. doi:10.1021/acsbiomaterials.7b00308.

[12] M. N. Silberstein, C. L. Pai, G. C. Rutledge, M. C. Boyce, Elasticplastic behavior of non-woven fibrous mats, Journal of the Mechanics and Physics of Solids 60 (2012) 295–318. doi:10.1016/j.jmps.2011.10.007.

[13] R. De Vita, D. J. Leo, K. D. Woo, C. Nah, A constitutive law for poly(butylene terephthalate) nanofibers mats, Journal of Applied Polymer Science 102 (2006) 5280–5283. doi:10.1002/app.24784.

[14] D. Wong, E. Verron, A. Andriyana, B. C. Ang, Constitutive modeling of randomly oriented electrospun nanofibrous membranes, Continuum Mechanics and Thermodynamics 31 (2019) 317–329. doi:10.1007/s00161-018-0687-x.

[15] O. Bas, S. Lucarotti, D. D. Angella, N. J. Castro, C. Meinert, F. M. Wunner, E. Rank, G. Vozzi, T. J. Klein, I. Catelas, E. M. De-Juan-Pardo, D. W. Hutmacher, Rational design and fabrication of multiphasic soft network composites for tissue engineering articular cartilage: A numerical model-based approach, Chemical Engineering Journal 340 (2018) 15–23. doi:10.1016/j.cej.2018.01.020.

[16] T. Courtney, M. S. Sacks, J. Stankus, J. Guan, W. R. Wagner, Design and analysis of tissue engineering scaffolds that mimic soft tissue mechanical anisotropy, Biomaterials 27 (2006) 3631–3638. doi:10.1016/j.biomaterials.2006.02.024.

[17] S. Mohammadzadehmoghadam, Y. Dong, I. J. Davies, Modeling electrospun nanofibers: An overview from theoretical, empirical, and numerical approaches, International Journal of Polymeric Materials and Polymeric Biomaterials 65 (2016) 901–915. doi:10.1080/00914037.2016.1180617.

[18] T. Stylianopoulos, C. A. Bashur, A. S. Goldstein, S. A. Guelcher, V. H. Barocas, Computational predictions of the tensile properties of electrospun fibre meshes: Effect of fibre diameter and fibre orientation, Journal of the Mechanical Behavior of Biomedical Materials 1 (2008) 326–335. doi:10.1016/j.jmbbm.2008.01.003.

[19] G. Argento, M. Simonet, C. W. J. Oomens, F. P. T. Baaijens, Multi-scale mechanical characterization of scaffolds for heart valve tissue engineering, Journal of Biomechanics 45 (2012) 2893–2898. doi:10.1016/j.jbiomech.2012.07.037.

[20] X. Wei, Z. Xia, S. C. Wong, A. Baji, Modelling of mechanical properties of electrospun nanofibre network, International Journal of Experimental and Computational Biomechanics 1 (2009) 45. doi:10.1504/IJECB.2009.022858.

[21] A. D'Amore, J. A. Stella, W. R. Wagner, M. S. Sacks, Characterization of the complete fiber network topology of planar fibrous tissues and scaffolds, Biomaterials 31 (2010) 5345–5354. doi:10.1016/j.biomaterials.2010.03.052.

[22] D. E. Caballero, F. Montini-Ballarin, J. M. Gimenez, S. A. Urquiza, Multiscale constitutive model with progressive recruitment for nanofibrous scaffolds, Journal of the Mechanical Behavior of Biomedical Materials 98 (2019) 225–234. doi:10.1016/j.jmbbm.2019.06.017.

[23] M. Zündel, E. Mazza, A. E. Ehret, A 2.5D approach to the mechanics of electrospun fibre mats, Soft Matter 13 (2017) 6407–6421. doi:10.1039/c7sm01241a.

[24] C. L. Pai, M. C. Boyce, G. C. Rutledge, On the importance of fiber curvature to the elastic moduli of electrospun nonwoven fiber meshes, Polymer 52 (2011) 6126–6133. doi:10.1016/j.polymer.2011.10.055.

[25] A. D'Amore, N. Amoroso, R. Gottardi, C. Hobson, C. Carruthers, S. Watkins, W. R. Wagner, M. S. Sacks, From single fiber to macro-level mechanics: A structural finite-element model for elastomeric fibrous biomaterials, Journal of the Mechanical Behavior of Biomedical Materials 39 (2014) 146–161. doi:10.1016/j.jmbbm.2014.07.016.

[26] J. Hu, W. Chen, B. Zhao, K. Wang, Uniaxial tensile mechanical properties and model parameters determination of ethylene tetrafluoroethylene (ETFE) foils, Construction and Building Materials 75 (2015) 200–207. doi:10.1016/j.conbuildmat.2014.10.017.

[27] M. S. Rizvi, P. Kumar, D. S. Katti, A. Pal, Mathematical model of mechanical behavior of micro/nanofibrous materials designed for extracellular matrix substitutes, Acta Biomaterialia 8 (2012) 4111–4122. doi:10.1016/j.actbio.2012.07.025.

[28] M. S. Rizvi, A. Pal, Statistical model for the mechanical behavior of the tissue engineering non-woven fibrous matrices under large deformation, Journal of the Mechanical Behavior of Biomedical Materials 37 (2014) 235–250. doi:10.1016/j.jmbbm.2014.05.026.

[29] P. L. Chandran, V. H. Barocas, Affine versus non-affine fibril kinematics in collagen networks: theoretical studies of network behavior, Journal of Biomechanical Engineering (2006) 259–270. doi:10.1115/1.2165699.

[30] T. Stylianopoulos, V. H. Barocas, Volume-averaging theory for the study of the mechanics of collagen networks, Computer Methods in Applied Mechanics and Engineering 196 (2007) 2981–2990. doi:10.1016/j.cma.2006.06.019.

[31] R. Inai, M. Kotaki, S. Ramakrishna, Structure and properties of electrospun PLLA single nanofibres, Nanotechnology 16 (2005) 208–213. doi:10.1088/0957-4484/16/2/005.

[32] E. P. Tan, S. Y. Ng, C. T. Lim, Tensile testing of a single ultrafine polymeric fiber, Biomaterials 26 (2005) 1453–1456. doi:10.1016/j.biomaterials.2004.05.021.

[33] E. P. S. Tan, C. T. Lim, Effects of annealing on the structural and mechanical properties of electrospun

polymeric nanofibres, Nanotechnology 17 (2006) 2649–2654. doi:10.1088/0957-4484/17/10/034.

[34] F. Chen, X. Peng, T. Li, S. Chen, X. F. Wu, D. H. Reneker, H. Hou, Mechanical characterization of single high-strength electrospun polyimide nanofibres, Journal of Physics D: Applied Physics 41 (2008). doi:10.1088/0022-3727/41/2/025308.

[35] S.-C. C. Wong, A. Baji, S. Leng, Effect of fiber diameter on tensile properties of electrospun poly(e-caprolactone), Polymer 49 (2008) 4713–4722. doi:10.1016/j.polymer.2008.08.022.

[36] H. Niu, H. Wang, H. Zhou, T. Lin, Ultrafine PDMS fibers: Preparation from in situ curing-electrospinning and mechanical characterization, RSC Advances 4 (2014) 11782–11787. doi:10.1039/c4ra00232f.

[37] J. Johnson, A. Ghosh, J. Lannutti, Microstructure-property relationships in a tissue-engineering scaffold, Journal of Applied Polymer Science 104 (2007) 2919–2927. doi:10.1002/app.25965.

[38] M. R. Roach, A. C. Burton, The reason for the shape of the distensibility curves of arteries, Canadian journal of biochemistry and physiology 35 (1957) 681–690. doi:doi.org/10.1139/o57-080.

[39] M. L. Raghavan, E. S. da Silva, Mechanical properties of AAA tissue, in: Biomechanics and Mechanobiology of Aneurysms, Springer, 2011, pp. 139–162.

[40] J. B. Carleton, A. D'Amore, K. R. Feaver, G. J. Rodin, M. S. Sacks, Geometric characterization and simulation of planar layered elastomeric fibrous biomaterials, Acta Biomaterialia 12 (2015) 93–101. doi:10.1016/j.actbio.2014.09.049.

[41] F. Montini Ballarin, P. C. Caracciolo, E. Blotta, V. L. Ballarin, G. A. Abraham, Optimization of poly(l-lactic acid)/segmented polyurethane electrospinning process for the production of bilayered small-diameter nanofibrous tubular structures, Materials Science and Engineering C 42 (2014) 489–499. doi:10.1016/j.msec.2014.05.074.

[42] R. Cintron, V. Saouma, Strain measurements with the digital image correlation system vic-2d, System 106 (2008) 1–22.

[43] V. Cnudde, M. Boone, High-resolution X-ray computed tomography in geosciences: A review of the current technology and applications, Earth-Science Reviews 123 (2013) 1–17. doi:10.1016/j.earscirev.2013.04.003.

[44] U. Stachewicz, P. K. Szewczyk, A. Kruk, A. H. Barber, A. Czyrska-Filemonowicz, Pore shape and size dependence on cell growth into electrospun fiber scaffolds for tissue engineering: 2D and 3D analyses using SEM and FIB-SEM tomography, Materials Science and Engineering: C 95 (2019) 397–408. doi:10.1016/j.msec.2017.08.076.

[45] K. L. Billiar, M. S. Sacks, Biaxial Mechanical Properties of the Natural and Glutaraldehyde Treated Aortic Valve Cusp—Part I: Experimental Results, Journal of Biomechanical Engineering 122 (2000) 23–30. doi:10.1115/1.429624.

[46] M. Schwartz, P. Leo, J. Lewis, A microstructural model for the elastic response of articular cartilage, Journal of Biomechanics 27 (1994) 865–873. doi:10.1016/0021-9290(94)90259-3.

[47] E. M. Arruda, M. C. Boyce, A three-dimensional constitutive model for the large stretch behavior of rubber elastic materials, Journal of the Mechanics and Physics of Solids 41 (1993) 389 – 412. doi:10.1016/0022-5096(93)90013-6.

[48] P. R. Cortez Tornello, P. C. Caracciolo, T. R. Cuadrado, G. A. Abraham, Structural characterization of electrospun micro/nanofibrous scaffolds by liquid extrusion porosimetry: A comparison with other techniques, Materials Science and Engineering C (2014). doi:10.1016/j.msec.2014.04.065.

[49] A. Morel, S. Domaschke, V. U. Kumaran, D. Alexeev, A. Sadeghpour, S. N. Ramakrishna, S. J. Ferguson, R. M. Rossi, E. Mazza, A. E. Ehret, et al., Correlating diameter, mechanical and structural properties of poly (l-lactide) fibres from needleless electrospinning, Acta Biomaterialia 81 (2018) 169–183. doi:10.1016/j.actbio.2018.09.055.

[50] J. A. Stella, W. R. Wagner, M. S. Sacks, Scale-dependent fiber kinematics of elastomeric electrospun scaffolds for soft tissue engineering, Journal of Biomedical Materials Research Part A 93 (2010) 1032–1042. doi:10.1002/jbm.a.32593.

- Micromechanical model for fiber interaction, recruitment and reorientation is presented
- A virtual deposition algorithm that mimics the electrospinning process is used
- Elastic-plastic constitutive law for the nanofibers is implemented
- Complex material macroscopic behavior is explained with simple microscopic phenomena
- The model could predict the macroscopic mechanical response of electrospun networks

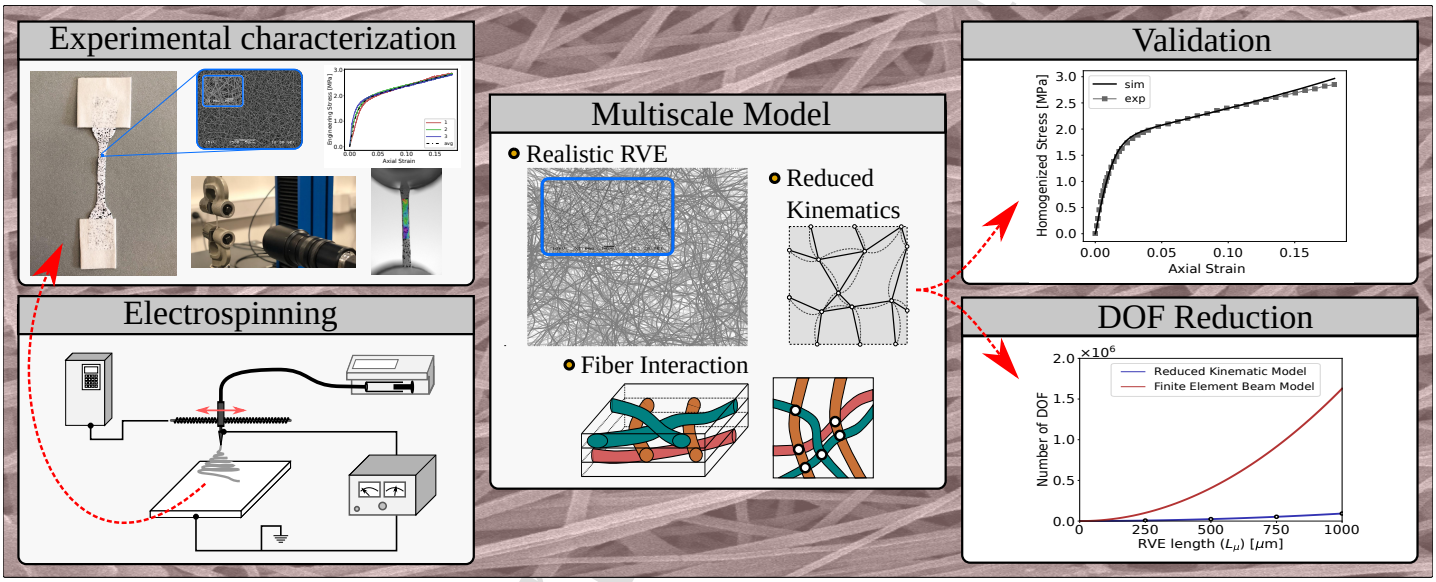

December 21, 2021

Av. Juan B. Justo 4302
Mar del Plata, Argentina
Tel: 54-0223-481-6600
Email: surquiza@fi.mdp.edu.ar

CRediT statements:

Daniel Caballero: Conceptualization, Methodology, Software, Validation, Formal analysis, Investigation, Visualization, Writing - Original Draft

Florencia Montini Ballarin: Conceptualization, Resources, Investigation, Writing - Review & Editing, Funding acquisition

Juan Manuel Gimenez: Software, Investigation, Visualization

Nicolás Biocca: Software, Investigation, Visualization

Nahuel Rull: Resources, Investigation

Patricia Frontini: Investigation, Resources, Methodology, Project administration, Funding acquisition

Santiago Adrián Urquiza: Conceptualization, Methodology, Project administration, Supervision, Funding acquisition, Writing - Review & Editing

I ensure that the descriptions are accurate and agreed by all authors.

Sincerely yours,

Dr. Santiago A. Urquiza
Grupo de Ingeniería Asistida por Computadora
Facultad de Ingeniería
Universidad Nacional de Mar del Plata

Declaration of interests

☒ The authors declare that they have no known competing financial interests or personal relationships that could have appeared to influence the work reported in this paper.

☐ The authors declare the following financial interests/personal relationships which may be considered as potential competing interests: